Development and characterisation of a turbulent boundary layer facility at the Delft University of Technology

Knoop, Max W.; Hassanein, A.H.; Baars, W.J.

DOI
10.1016/j.ast.2025.110972

Publication date
2025

Document Version
Final published version

Published in
Aerospace Science and Technology

Citation (APA)
Knoop, M. W., Hassanein, A. H., & Baars, W. J. (2025). Development and characterisation of a turbulent boundary layer facility at the Delft University of Technology. *Aerospace Science and Technology*, *168*, Article 110972. https://doi.org/10.1016/j.ast.2025.110972

Aerospace Science and Technology 168 (2026) 110972

Contents lists available at ScienceDirect

Aerospace Science and Technology

journal homepage: www.elsevier.com/locate/aescte

Original article

Development and characterisation of a turbulent boundary layer facility at the Delft University of Technology

Max W. Knoop *, Abdelrahman Hassanein , Woutijn J. Baars

Faculty of Aerospace Engineering, Delft University of Technology, Delft, 2628 HS, The Netherlands

ARTICLE INFO

Communicated by Cummings Russell

Keywords:
Wall-bounded turbulence
Turbulent boundary layer facility
High friction Reynolds number

ABSTRACT

A new facility for studying turbulent boundary layer flows has been developed at the Delft University of Technology and is referred to as the DU-BLF: Delft University Boundary Layer Facility. Its design and boundary layer data characteristics are presented in the current work. The DU-BLF can be employed for a range of studies revolving around boundary layer flows, *e.g.*, covering fundamentals of boundary layer development, flow control with passive surface modifications, and control efforts with active technologies. A modular setup of the test section allows for a relatively long development length, with both physical and optical access over its complete extent. For the present characterisation, a turbulent boundary layer was developed under a zero (streamwise) pressure gradient, with the aid of a flexible ceiling. We establish the general flow characteristics, including freestream turbulence intensity levels, acoustic noise characteristics, boundary layer-integral parameters, and wall-normal profiles of the first and second-order turbulence statistics. Results are validated by employing multiple measurement techniques, namely, hot wire anemometry, particle image and tracking velocimetry, and wall-pressure measurements. Results are shown for friction Reynolds numbers up to $Re_\tau \approx 5\,100$, and reveal that the boundary layer flow adheres to the expected behaviour of canonical wall-bounded turbulence. Data of the current turbulent boundary layer measurements are made available online.

1. Introduction

Wall-bounded turbulence is a widely observed phenomenon which has been studied extensively over the past 150 years [1]. Characterising, describing, and understanding its self-sustaining mechanisms has proven to be a major task, also because its details are strongly dependent on the imposed flow conditions by, for instance, an external pressure gradient or the nature of the wall (*e.g.*, smooth or rough, flat or curvilinear surfaces). Experimental simulations of practically relevant turbulent boundary layer (TBL) flows are still advancing our fundamental understanding and ability to control these flows; this will eventually lead to efficient engineering systems [2]. In particular, we are interested in the study of moderate to high Reynolds number TBL flows, with friction Reynolds numbers of order $Re_\tau = \mathcal{O}(10^3)$ to $\mathcal{O}(10^6)$ as these occur commonly in practical applications, like the aerospace or maritime transportation sector.

High Reynolds number flows present a significant scale separation between the inner-scale (viscous length scale, l_v) and outer-scale (boundary layer thickness, δ), represented by $Re_\tau \equiv U_\tau \delta/\nu = \delta/l_v$, where the friction velocity is defined as $U_\tau \equiv \sqrt{\tau_w/\rho}$ with τ_w being the wall-shear-stress, and ρ and ν being the fluid's density and kinematic viscosity, respectively (note that quantities that are scaled with the viscous parameters are denoted with a '+' superscript). As the scale separation increases (*i.e.* $\propto Re_\tau$), the dynamics of near-wall turbulence, already present in low Re_τ flows, are complexified by the co-existing larger-scale motions [3]. Hence, studying wall-bounded turbulence with a broadband range of scales is needed, *e.g.*, from the perspective of statistically describing the organisation of scales [4], or from the perspective of developing large-scale control [5,6].

Experimentally achieving high values of Re_τ, while retaining a sufficient measurement resolution in terms of the viscous length and time scales, is not trivial. To address this, the scientific community has made efforts to extend the development length of the TBL to accommodate the growth of δ while keeping l_v in a measurable range. For instance, Österlund [7] achieved $Re_\tau \approx 7\,000$ at a development length of 5.5 m in the MTL facility at the KTH Royal Institute of Technology; similarly, at a development length of 9 m, Aguiar Ferreira et al. [8] attained $Re_\tau \approx 8\,000$ in the boundary layer wind tunnel at the University of Southampton; a longer working section allowed for $Re_\tau \approx 20\,000$ at a development length of 21 m within the University of Melbourne's boundary layer facility [9]. Following the same design principle—of developing a high Reynolds number flow with a relatively long development length—the

* Corresponding author.
E-mail address: m.w.knoop@tudelft.nl (M.W. Knoop).

https://doi.org/10.1016/j.ast.2025.110972
Received 11 May 2025; Received in revised form 30 July 2025; Accepted 19 September 2025
Available online 25 September 2025

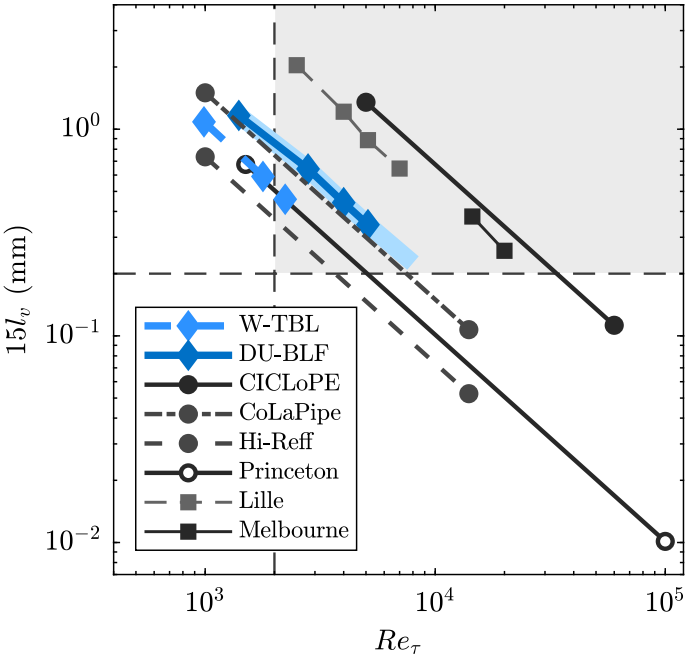

Fig. 1. A selection of airflow facilities used for measurements of wall-bounded turbulence, in terms of their typical operating range of friction Reynolds number, Re_τ, and viscous length scale, l_v (the ordinate of $15l_v$ reflects the physical wall-normal distance of the inner-peak in $\overline{uu}$). Two facilities at the Delft University of Technology are considered: the W-TBL setup [6] and the current DU-BLF. Reference facilities include high Reynolds number pipe flow facilities [CICLoPE [10–12], CoLaPipe [13], Hi-Reff [14], Princeton Superpipe [15]] and high Reynolds number turbulent boundary layer facilities [Lille [16], Melbourne [17]].

Delft University Boundary Layer Facility (DU-BLF) was commenced, with a test section length of ~ 7.2 m, double that of a previous boundary layer facility [6].

To place our facility in context, it is instructive to summarise the high-level capabilities of facilities designed for the study of wall-bounded turbulence. For this, one can consider the range of Re_τ that can be obtained while considering the corresponding viscous length scale in absolute units. Fig. 1 presents a map of $15l_v$ (representative of the physical wall-normal distance of the inner-peak in $\overline{uu}$) versus Re_τ, populated with curves resembling the operation of several facilities. These curves represent a fixed measurement location, corresponding to the largest streamwise development length, while the bulk velocity is varied. Only combinations of l_v and Re_τ on the left-bottom-side of the trend lines can be achieved (considering that measurements can be performed at streamwise locations with a reduced development length). The highest Re_τ value of each trendline is facility-limited, while the lower limit is not necessarily an operating limit but may correspond to the lowest Re_τ at which data was reported in the cited works (see caption of Fig. 1). Our facility neither operates in an unexplored flow regime (*e.g.*, very high Re_τ domains), nor does it provide an unprecedented viscous length scale to allow for fully-resolved measurements. However, the DU-BLF operates in a Reynolds number range that is relevant to study the dynamics of high Reynolds number TBL flows governed by a range of coherent structures [18,19, among others]. That is, at Re_τ values of several thousands, the logarithmic layer is well-established and spans a full decade at the largest Re_τ design point of $Re_\tau \approx 8\,000$. This full operational range is indicated by the light blue shaded patch in Fig. 1 and considers a closed-loop design with the maximum power of the axial fan dictating the operating limit. Though, for the present study, an open-loop configuration is considered because of current building/space limitations. In this configuration, the maximum operating velocity results in $Re_\tau \approx 5\,100$; the four operational points considered in the current paper are shown with the diamond markers in Fig. 1. Aside from the reasonable Re_τ range, the viscous length scale is kept large enough ($15l_v \gtrsim 0.2$ mm) to resolve near-wall turbulence with off-the-shelf hot wires or optical-based measurement techniques.

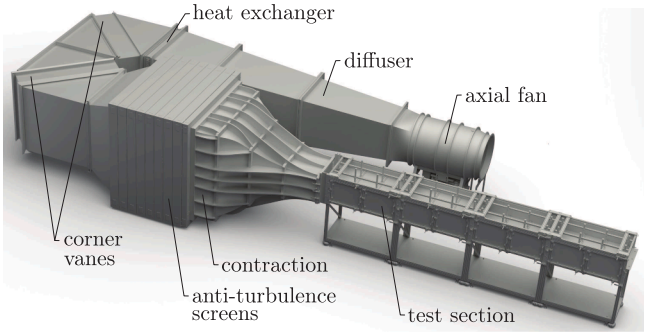

Fig. 2. CAD impression of the DU-BLF with an annotation of the primary components.

The present contributions of the paper are as follows. We present design details of the DU-BLF and its key characteristics relevant for experimental studies (Section 2). Facility characteristics and turbulence statistics are measured with various techniques, including hot wire anemometry (HWA), particle image velocimetry (PIV), particle tracking velocimetry (PTV), and static and time-resolved pressure measurements, described in Section 3. Facility and boundary layer data are presented in Section 4, considering, among other things, the freestream turbulence and acoustics, the quality of the zero streamwise pressure gradient, and the turbulence statistics.

2. Design of the facility

The new DU-BLF is integrated into a low-turbulence tunnel at the Delft University of Technology, schematically shown in Fig. 2. Parts of the tunnel facility—notably the diffuser downstream of the axial fan, the corner vanes, and the anti-turbulence screens—were reused from a dismantled facility known as the boundary layer tunnel at the Low Speed Aerodynamics laboratory of the Delft University of Technology [see Section 3.4.1 in 20]. The current tunnel can be configured in a closed- or open-loop configuration, and in the current work, we consider an open-loop setup. The tunnel is powered by a 75 kW axial fan, with a maximum rotation rate of 1 200 RPM, as such, achieving a maximum freestream velocity at the outlet of the contraction of ~ 30 m/s (in the open-loop configuration). A heat-exchanger is installed for testing under stable temperature conditions. After two corner vane sections, a total of seven anti-turbulence screens in the plenum aid a low level of freestream turbulence intensity (see Section 4.1). The flow quality is also enhanced with the aid of a contraction with an 11:1 area ratio, comprising an outlet area of $L \times H = 0.9 \times 0.6$ m^2, where L and H are the width and height, respectively. Along with a canonical TBL developing under a zero pressure gradient (ZPG) in the streamwise direction, the facility's versatility permits the study of a wide variety of other flow cases, *e.g.*, boundary layer flows subject to pressure gradients or ones subject to passive or active flow control.

The working section with a cross-sectional area of 0.9×0.5 m^2 (span × height) has a streamwise length of approximately 7.3 m, consisting of four individual 1.8-m-long sections (numbered 1 to 4 in Fig. 3a). A side-view schematic of the test section is depicted in Fig. 3(a), with alongside in Fig. 3(b) a photograph from the downstream end of the test section. The design considerations and key features are laid out below:

- For boundary layer studies, the TBL is generated on the suspended flat-plate floor, comprising an elliptical leading edge located ~ 100 mm above the bottom wall of the contraction outlet (Fig. 3a,c). A diffuser plate is used to effectively bleed the air below the floor,

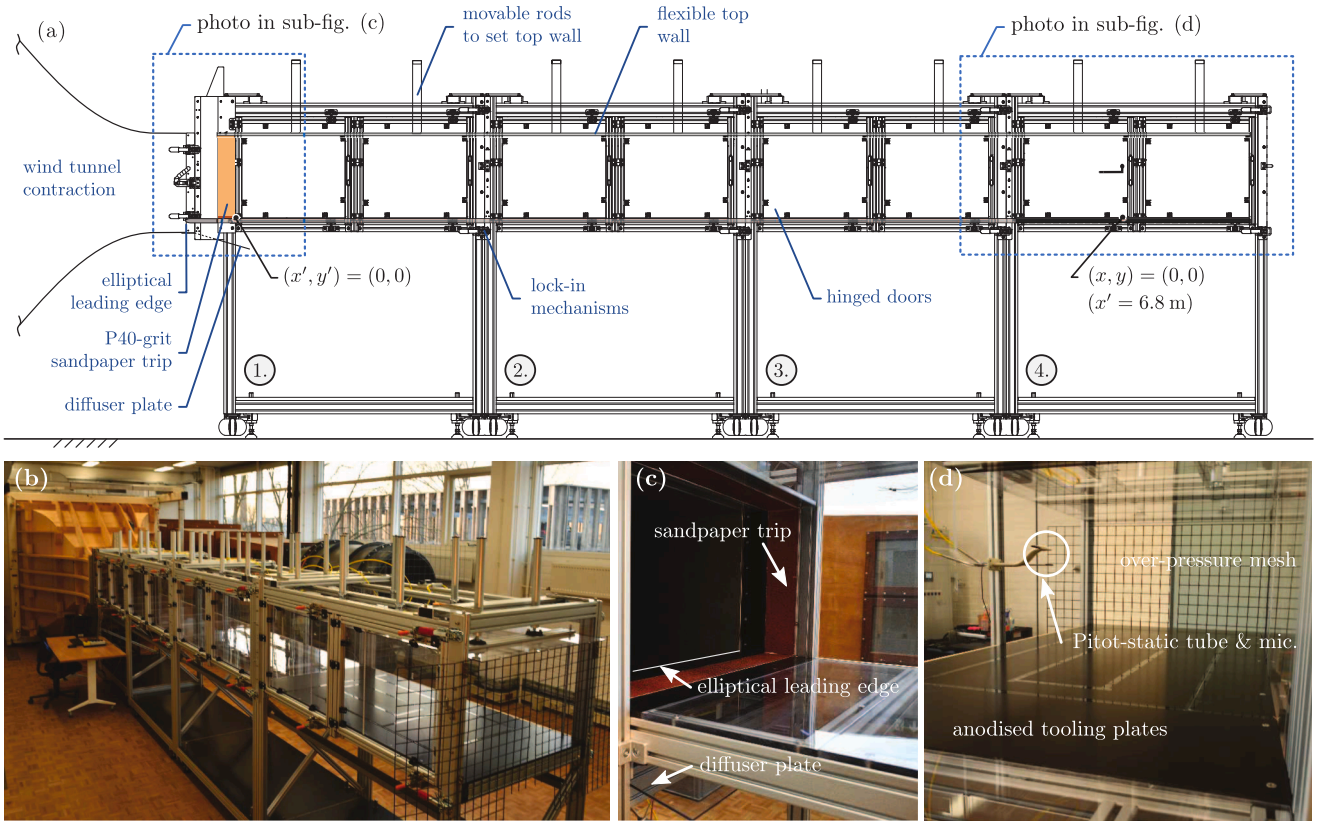

Fig. 3. (a) Schematic of the Delft University Boundary Layer Facility (DU-BLF). Several features of the facility are highlighted by means of photographs: (b) overview of the DU-BLF test section, (c) detail of the test section inlet, and (d) close-up of test-section 4 designed for measurements.

preventing unwanted separation on the overlying TBL. The boundary layer is tripped to a turbulent state by a 120 mm strip of P40-grit sandpaper applied all around the wall perimeter of test-section 1.

- The test section comprises a flexible top wall to achieve a certain streamwise pressure gradient (see Fig. 3a,b). Scales are included on the sidewalls to position the ceiling profile with an accuracy of ~ 1 mm. Pressure gradients can be quantified with 126 wall-normal static pressure taps, embedded in the bottom wall with a nominal streamwise spacing of 50 mm.
- Full physical and optical access along the streamwise direction is provided (Fig. 3b), offering ample opportunity for optically based measurements. All test sections were constructed out of lightweight extruded aluminium profiles with the walls of the working sections made out of 12 mm thick transparent polycarbonate. Each test section has two hinged doors on one of its sides.
- Test-section 4 (Fig. 3d) is specifically designed for conducting TBL studies. A Pitot-static tube and a microphone are installed on the side wall to measure the freestream velocity and acoustic pressure, respectively. This section is equipped with a floor consisting of multiple panels, allowing for the insertion of test plates in an insert area of 1200×600 mm (in the streamwise and spanwise directions). Nominally, two test plates are installed (plates of 800×600 mm and 400×600 mm in size, each with a thickness of 12 mm); the larger one can accommodate a smaller insert of 600×220 mm with a thickness of 10 mm. Typically, a matt black anodisation is applied to the aluminium tooling plates to prevent strong laser-light reflections when performing near-wall laser-based measurements. In addition, the tunnel floor of test-section 3 allows for the insertion of a flush-mounted, direct force balance system of Van Nesselrooij et al. [21]. Note that test-section 2 to 4 can be interchanged to vary the streamwise development length upstream of the measurement station.
- The outlet is equipped with a mesh, generating an over-pressure with respect to the ambient in the working section, making it less sensitive to outside variations in pressure. Moreover, by changing the mesh configuration and setting the ceiling height, TBL flows with streamwise pressure gradients can be achieved.

3. Experimental details

Here we detail the experimental methodology employed to characterise the TBL flow in the DU-BLF. We establish a Cartesian coordinate system, originating at the measurement location, with (x, y, z), denoting the respective streamwise, wall-normal, and spanwise directions, corresponding to the instantaneous velocity components (U, V, W). A global coordinate system (x', y', z'), denoted with prime superscripts, has its origin at the tunnel centreline and coincides with the downstream edge of the P40-grit sandpaper trip. Standard Reynolds averaging is applied where the capitalised quantity with an overline, and the lowercase quantity, denote the temporally- or spatially-averaged mean and fluctuating components, respectively, *e.g.*, $U = \overline{U} + u$.

Measurements were conducted at two streamwise locations: (1) at the outlet plane of the contraction (near $x' = 0$), and (2) within test-section 4 at the nominal measurement location of $x' = 6.8$ m (which coincides with the origin of the x, y, z coordinate system). In addition, a characterisation of the pressure gradient along the full length of the working section was conducted. An overview of the respective measurements is provided in Table 1. Experiments were conducted at four nominal freestream velocities of $U_\infty \approx 5,\ 10,\ 15$, and 20 m/s (corresponding colours of lines/markers for differentiating the associated data in the graphs are indicated in Table 1). At both aforementioned measurement locations, HWA measurements were conducted (details are presented in Section 3.1) to characterise the freestream turbulence intensity. The

Table 1
Overview of the conducted measurements at their respective x' locations. We present the colour scheme associated with the individual methods, where the colour gradient denotes increasing streamwise velocity from $U_\infty \approx 5$ to 20 m/s.

Method	x' location (m)	U_∞ (m/s)	Colour
HWA	0, 6.8	5	
		9.9	
		14.9	
		19.8	
PIV	6.8	4.6	
		9.2	
		13.7	
		18.3	
PTV	6.8	4.6	
		9.2	
		13.7	
		18.3	
Wall-pressure & background acoustics	6.8	5	
		10	
		15	
		20	
Streamwise pressure gradient	0.65-7.2	5	
		10	
		15.2	
		20.1	

Table 2
Overview of the measurement characteristics during the HWA experiment. The viscous length and time scales are defined as $l_v^+ \equiv \nu/U_\tau$ and $t_v^+ \equiv \nu/U_\tau^2$, respectively.

U_∞ (m/s)	l_v (μm)	t_v (μs)	l^+	Δt^+	TU_∞/δ
5	77.7	394	16.1	0.05	4 640
10	42.8	119	29.2	0.16	8 350
15	29.4	56.1	42.5	0.35	12 600
20	23.0	33.7	54.3	0.58	16 800

Table 3
Imaging conditions and processing parameters for the separate PIV- and PTV-based measurement techniques. The vector pitch range corresponds to the lowest and highest freestream velocity considered ($U_\infty = 5$ and 20 m/s, respectively).

	PIV	PTV
Field-of-view	169×209 mm^2	21.0×17.6 mm^2
	$\sim 1.6 \times 1.9\ \delta^2$	$\sim 0.19 \times 0.15\ \delta^2$
Image resolution	14.0 px/mm	125.0 px/mm
Interrogation/binning window	32×8 px^2	8×8 px^2
Processing technique	cross-correlation	PTV
Overlap	75 %	75 %
Vector pitch	0.26 mm	0.016 mm
	$3.2 - 11.2\ \nu/U_\tau$	$0.19 - 0.68\ \nu/U_\tau$

TBL flow (at $x' = 6.8$ m) was characterised by means of HWA, and PIV and PTV (described in Section 3.2). Moreover, the background acoustics and wall-pressure were also characterised at this location (Section 3.3). Lastly, the boundary layer's ZPG was assessed through wall-based static pressure measurements (Section 3.3) over the full streamwise development length.

3.1. Hot wire anemometry

For time-resolved streamwise velocity measurements, a Dantec 55P15 miniature boundary layer probe was employed with a TSA IFA-300 constant temperature anemometer. Conduction-based attenuation through the prongs is minimised by having a sufficient length-to-diameter ratio $l/d = 250$ [22], with $d = 5$ μm and $l = 1.25$ mm. Time series were acquired for a duration of $T = 100$ s, at a sampling frequency of $f_s = 51.2$ kHz. In Table 2, we provide the viscous wire length (l^+), viscous time separation ($\Delta t^+ = 1/f_s^+$), and the acquisition length of the time series in terms of boundary layer turnovers (TU_∞/δ). An analogue low-pass filter of 20 kHz was applied to the voltage signal before A/D conversion with a 24-bit NI 9234 DAQ module. In-situ calibration was performed by fitting a fourth-order polynomial to 17 points of streamwise velocity in the range $U_\infty \in [1.5, 23]$ m/s. Drifts in ambient temperature were corrected following the methodology of Hultmark and Smits [23]. Wall-normal profiles of the streamwise velocity were acquired by employing a 300 mm Zaber X-LRQ traversing system (10 μm step accuracy). A total of 40 logarithmically-spaced wall-normal locations were sampled, ranging from approximately 0.1 mm to 210 mm ($\sim 1.8\delta$). The wall-normal location of the HWA probe was determined using the camera from the PTV setup. In processing the streamwise velocity profiles, the wall-normal position is more accurately determined by including a Δy shift to the composite fitting procedure [24,25]. For statistical convergence of velocity spectra, we applied ensemble averaging with ensembles of $N = 2^{15}$ samples at a 50 % overlap, each weighted with a Hanning window; this yields a spectral resolution of $\mathrm{d}f \approx 1.56$ Hz.

3.2. Two-component velocity field measurements

To capture turbulence statistics, planar two-dimensional two-component (2D2C) velocity field measurements were conducted in the streamwise–wall-normal plane ($x - y$), centred at $x' = 6.8$ m. PIV and PTV were performed, and for both cases, a total of 2 000 image pairs were acquired at a frequency of 15 Hz. Imaging was performed using one LaVision Imager sCMOS CLHS camera with a 12-bit sensor, comprising a resolution of 2560 × 2160 px^2, and a pixel size of 6.5 μm. Atomised glycol water was used to inject ~ 1 μm flow tracer particles.

For the PIV experiment, we sought to capture the full wall-normal extent of the TBL. The camera was mounted with 200 mm Nikkor-AF objectives at an aperture of f/8. The resulting field-of-view (FOV) was 169×209 mm^2 ($\sim 1.6 \times 1.9\ \delta^2$), in the x- and y-directions, respectively, and comprised a resolution of 14.0 px/mm. Image analysis was performed in LaVision DaVis 10.2 software, employing a multi-pass cross-correlation algorithm [26] with an adaptive window deformation method [27]. A final window pass of 32 × 8 px^2 with a 75 % overlap was employed, resulting in a vector pitch of ~ 0.26 mm.

The aim of the PTV measurement was to infer the wall-shear stress, and concurrently the viscous-scaling parameters, from a direct measurement of $d\overline{U}/dy$ in the viscous layer. We employed a 200 mm Nikkor-AF objective at f/8, in combination with a 2× teleconverter for doubling the magnification. This resulted in a FOV of 21.0×17.6 mm^2 ($\sim 0.19 \times 0.15\ \delta^2$), in the x- and y-directions, respectively, and a resolution of 125 px/mm. PTV was performed in DaVis 10.2, after which the particle tracks were binned in windows of 8×8 px^2 with 75 % overlap, resulting in a vector pitch of ~ 0.016 mm. To summarise, we present the details of the imaging conditions, viscous scaling, and analysis parameters in Table 3.

3.3. Pressure measurements

In order to assess the streamwise pressure gradient, mean static pressure measurements were conducted with 40 pressure taps embedded within the bottom wall of the test section, spanning a streamwise fetch of $x' \approx 0.65$ to 7.2 m. Their streamwise spacing is nominally 150 mm, and occasionally reaches a maximum spacing of 350 mm because of the junctions between the four test sections. The mean total pressure was acquired with the aid of a Pitot-static tube mounted to the tunnel's side wall at $x' \approx 6.8$ m.

Fluctuating pressure measurements were conducted using multiple GRAS 46BE 1/4-inch pressure microphones at $x' \approx 6.8$ m. One microphone was positioned in the external flow region to capture the acoustic

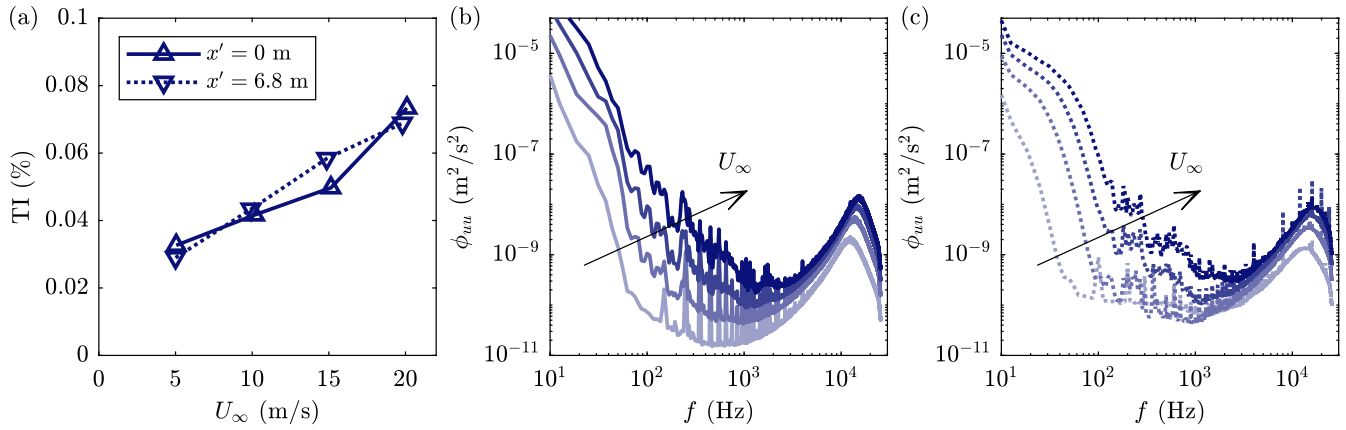

Fig. 4. (a) Turbulence intensity (TI) of the freestream streamwise velocity, corresponding to locations at the inlet of the contraction ($x' = 0$ m) and within the test section at the nominal measurement location ($x' = 6.8$ m), for $U_\infty \approx 5$ to 20 m/s. A 20 to 8 000 Hz band-pass filter was employed to remove low-frequency breathing and high-frequency anemometer noise. The corresponding energy spectra of the streamwise velocity fluctuations are presented in (b) for $x' = 0$ m, and in (c) for $x' = 6.8$ m.

noise, whereas five microphones were embedded as an array in the bottom wall to infer the TBL-induced wall-pressure fluctuations. The one in the external flow was equipped with a GRAS RA0022 1/4-inch nosecone to remove pressure fluctuations from the turbulence in the stagnation point [similar as used by 28]. For the wall-pressure measurements, all five microphones were mounted in a sub-surface cavity and communicated with the flow through a pinhole. Their equidistant spacing in the spanwise direction was 20 mm ($\sim 0.18\ \delta$). The pinhole–cavity dimensions were taken as follows: a pinhole orifice diameter of $d = 0.4$ mm (corresponding to $d^+ \approx 5$ to 17), a pinhole depth of $l = 1.0$ mm, a cavity diameter of $D = 6.0$ mm and a cavity length of $L = 2.0$ mm. This configuration resulted in a Helmholtz resonance frequency of $f_0 \approx 2\ 725$ Hz (or $f_0^+ \approx 1.1$ to 0.082). The measured pressure signals need to be corrected for the occurrence of Helmholtz resonance. This is done by considering a Helmholtz transfer kernel: this frequency-dependent relation relates the (measured) cavity pressure to the orifice-inlet pressure (the true wall-pressure). The correction itself is performed by dividing the spectra of the measured pressure signals by the gain of the Helmholtz transfer kernel [for details, see Appendix A in 28]. Because of the non-anechoic tunnel environment, acoustic noise also needs to be corrected for. At each time step, acoustic noise was removed by subtracting the spanwise mean of the wall-pressure across the microphone array. This approach assumes that the hydrodynamic (turbulence-induced) wall-pressure fluctuations are only energetic at spanwise scales smaller than the span of the array (roughly 0.9δ).

The microphone sets used had a nominal sensitivity of 3.6 mV/Pa, with an accuracy of ± 1 dB in the frequency range of 10 Hz to 40 kHz. The microphones' dynamic range spans 35 to 160 dB, based on a reference pressure of $p_{\text{ref}} = 20\ \mu Pa$. Sampling was performed using the same NI 9234 DAQ module and settings as those used for the HWA acquisition, except that time series were acquired for a total duration of $T = 750$ s for each freestream velocity. As for the hot-wire data, ensemble averaging was applied for generating wall-pressure spectra. Ensembles of $N = 2^{15}$ samples were taken at a 50 % overlap, each weighted with a Hanning window; this yields a spectral resolution of $\mathrm{d}f \approx 1.56$ Hz.

4. Facility and boundary layer data

In this section, we first consider the data characteristics associated with the external (inviscid) flow in the DU-BLF (freestream turbulence and ZPG assessment). Subsequently, data of the ZPG TBL will be presented. Throughout this section, we denote the respective measurements by their colour scheme indicated in Table 1; an increasing colour intensity indicates the trend with an increase in U_∞.

4.1. Freestream turbulence characteristics

We characterise the freestream turbulence intensity (TI) of the streamwise velocity fluctuations, defined as $\mathrm{TI} \equiv \sqrt{\overline{uu}}/\overline{U}$. Streamwise velocity measurements were acquired with HWA between $U_\infty \approx 5$ to 20 m/s, at the outlet plane of the contraction ($x' = 0$, without the working section installed) and the nominal measurement station with the working section installed ($x' = 6.8$ m). A digital filter with a band-pass range of 20 to 8 000 Hz was applied before computing the TI values. These lower and upper frequency bounds were chosen to remove any low-frequency breathing that does not affect the boundary layer, and spurious high-frequency energy attributable to the noise floor of the anemometer (see discussion below).

As shown in Fig. 4(a), the TI at both streamwise locations is positively correlated with U_∞, and increases from approximately 0.03 % to 0.07 %. Contrasted to other turbulent boundary facilities, *e.g.*, Marusic et al. [9] report turbulence intensities of 0.15 % to 0.2 %, whereas Dacome et al. [6] report 0.35 %. The TI slightly exceeds the TI < 0.03% range reported by Rius-Vidales and Kotsonis [29] for the Low Turbulence Tunnel at the Delft University of Technology. This tunnel was developed for laminar flow and transition studies, and we therefore consider the current TI to be of sufficient quality. The energy spectra of the velocity fluctuations (ϕ_{uu}) are presented in Fig. 4(b,c), for the two streamwise locations, respectively. As a function of U_∞, the spectral energy increases at both locations, corresponding to the monotonic increase in TI. In addition, regardless of the freestream velocity, a series of spectral peaks located at 150, 250, 350, …, 4 000 Hz, are attributed to low-magnitude electromagnetic noise as previously noted for the same anemometer by Merino-Martínez et al. [30]; moreover, their influence on the TI is negligible given their low magnitude and narrow spectral footprint.

4.2. Open-jet characterisation

To characterise the uniformity of the tunnel flow, the spatial variation in streamwise velocity was assessed within the open jet forming from the outlet plane of the contraction (without the working section installed). Using a Pitot-static tube, the mean streamwise velocity, $\overline{U}$, was measured at a nominal velocity of $U_\infty = 10$ m/s. The variation of $\overline{U}$ was characterised with 9 point measurements along $\hat{x}/H \in [0,\ 1.6]$ at $\hat{y} = \hat{z} = 0$ (exit height $H = 0.6$ m). Here $\hat{\cdot}$ denotes a coordinate system with its origin in the spanwise centre and mid-height of the contraction's outlet plane. The uniformity of the jet and the free shear later were characterised in one quadrant at $\hat{x}/H = 0.5$, comprising 13 and 11

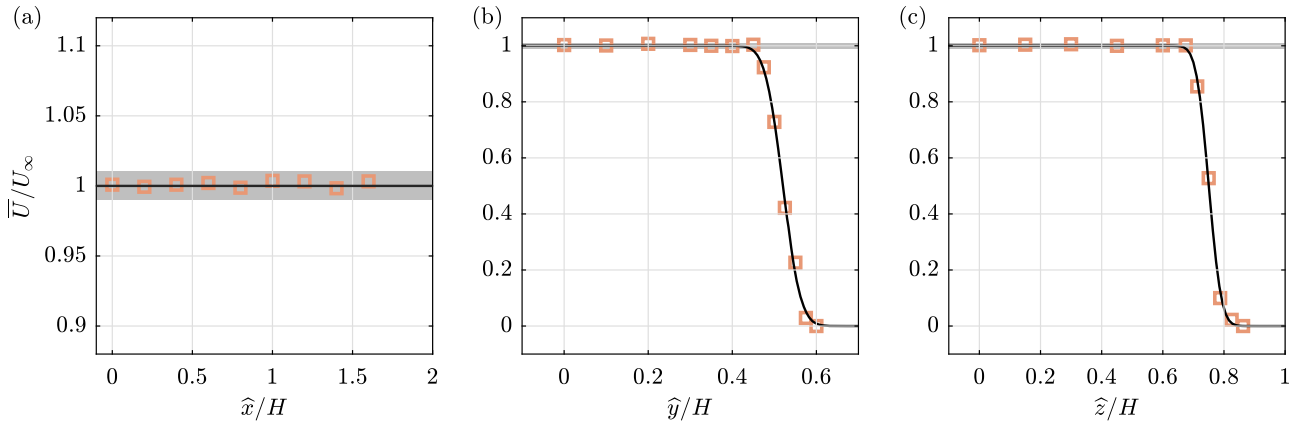

Fig. 5. Streamwise velocity profiles of the open jet at $U_\infty = 10\,\mathrm{m/s}$, (a) streamwise profile at the jet centreline ($\widehat{y} = \widehat{z} = 0$), (b) wall-normal profile at $\widehat{x} = 0.5H$, $\widehat{z} = 0$, and (c) spanwise profile at $\widehat{x} = 0.5H$, $\widehat{y} = 0$. Grey-shaded patches indicate the uncertainty interval $U_\infty \pm 1\,\%$. The black lines in (b,c) show the Görtler [31] fit following (1).

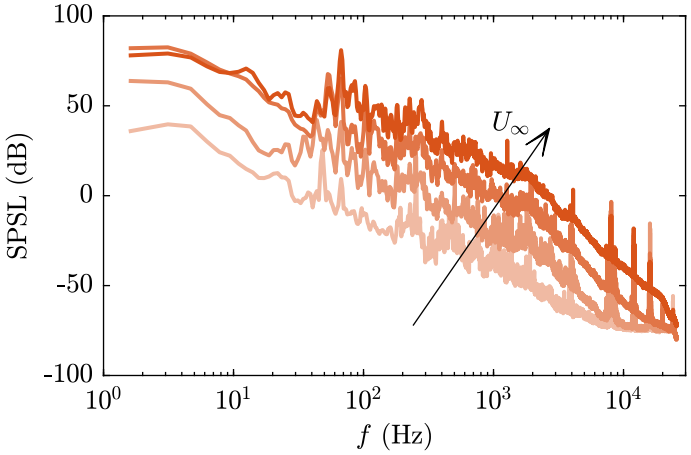

Fig. 6. Sound pressure spectrum level of the acoustic pressure measured in the freestream, for freestream velocities in the range $U_\infty \approx 5$ to $20\,\mathrm{m/s}$.

point measurements along $\widehat{y}/H \in [0,\ 0.6]$, and $\widehat{z}/H \in [0,\ 0.85]$, respectively.

A negligible variation of the $\overline{U}$ velocity in the potential core is shown in Fig. 5(a), where $\overline{U}$ remains within $U_\infty \pm 0.3\,\%$ (the grey shaded patch indicates $U_\infty \pm 1\,\%$). The spanwise and wall-normal profiles (Fig. 5b,c) reveal a variation of velocity in the potential core flow of less than $U_\infty \pm 0.5\,\%$. The black lines in Fig. 5(b,c) indicate that the open-jet shear layer is well represented by the semi-empirical model of Görtler [31], which provides a self-similar solution based on Prandtl's eddy viscosity hypothesis via a fitted model function:

$$\frac{\overline{U}}{U_\infty} = \frac{1}{2}\left[1 + \mathrm{erf}\left(\xi + \xi_0\right)\right]. \tag{1}$$

The self-similarity variable is represented by $\xi = \sigma\widehat{y}/\widehat{x}$ for the vertical profile along $\widehat{y}$ ($\sigma = 10.6$ represents the spreading rate of the shear layer, and $\xi_0 = 0.431$ accounts for the outward movement of the shear-layer centreline), or by $\xi = \sigma\widehat{z}/\widehat{x}$ for the spanwise profile along $\widehat{z}$ ($\sigma = 16.5$ and $\xi_0 = 0.007$).

With the inflow to the working section regarded as being nominally uniform in y- and z-directions, the flow inside the working section develops in a symmetric manner (the working section is fully symmetric by design). When considering the size of the working section, in terms of its dimensions normalised by the boundary layer thickness δ (here taken as $\delta = 110\,\mathrm{mm}$, see Section 4.5 below), the cross-sectional area is $\sim 8.2\delta \times 5.5\delta$ (span × height) at the most downstream measurement location of $x' \approx 62\delta$ ($x' = 6.8\,\mathrm{m}$). This size is regarded as sufficient for accurate TBL measurements without influences of the side/top walls, given its comparison to other facilities: *e.g.*, the facility in Lille has a cross-sectional area of $5.9\delta \times 2.9\delta$ (span × height) at a streamwise location of 58δ [following data of 16], and the facility in Melbourne has a cross-sectional area of $6.5\delta \times 3.3\delta$ (span × height) at a streamwise location of 67δ [following data of 17].

4.3. Background acoustic characteristics

The Sound Pressure Spectrum Level (SPSL) was used to assess the noise level in the tunnel, calculated from the energy spectrum of the pressure fluctuations (ϕ_{pp}), following:

$$\mathrm{SPSL}(f) = 20\log\left(\frac{\phi_{pp}(f)}{p_{\mathrm{ref}}^2}\right), \tag{2}$$

with $p_{\mathrm{ref}} = 20\ \mu Pa$. Fig. 6 presents the SPSL-based spectra for different freestream velocities. An increase in the SPSL is noticeable across all frequencies with an increase in freestream velocity. The background acoustics in the tunnel are predominantly broadband in nature and are most energetic in the low-frequency range (2 to 100 Hz). In addition, a minor tonal peak is observed with a frequency of 65 Hz for all freestream velocities.

4.4. Zero pressure gradient assessment

We assess the quality of the ZPG along the streamwise direction by considering the pressure coefficient, $C_p \equiv 1 - (U_e/U_\infty)^2$. Here, U_e is the local edge velocity of the TBL calculated from the static pressure ports, under the assumption of a zero-valued wall-normal pressure gradient. Fig. 7 presents streamwise profiles of C_p, and reveals that the variation in C_p is within $\pm 2\,\%$ (corresponding to a variation of $U_e \pm 1\,\%$) for all freestream velocities considered. Note that the static pressure for $x' \gtrsim 7\,\mathrm{m}$ is affected by the over-pressure mesh, as indicated by the grey markers. As such, we exclude these points from our assessment and consider measurements valid up to $x' = 6.8\,\mathrm{m}$. To quantify the ZPG, we make use of the acceleration parameter, $K \equiv (\nu/U_e^2)|(dU_e/dx)|$ [32]. The local value of which is kept to within $K < 1.3e-7$ along the entire working section for all operation conditions, whereas its median is of order $K \approx 1 \times 10^{-8}$ to 1×10^{-9}. Taking into account the available literature [*e.g.*, $K < 1.6 \times 10^{-7}$ and $K < 1 \times 10^{-8}$ for, 6,32, respectively], we deem these values sufficient to achieve ZPG development of the TBL flow. The ceiling height profile remains fixed when varying U_∞. As a result, there are minor variations of the acceleration parameter for each freestream velocity. However, these remain well within the acceptable limits for

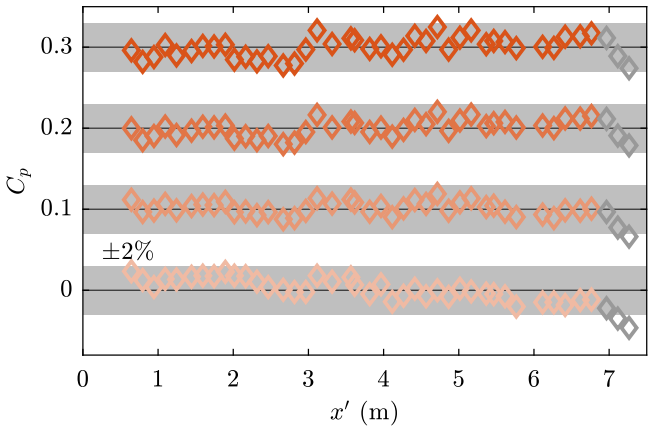

Fig. 7. Streamwise variation of the pressure coefficient. Data curves are consecutively offset in the vertical direction with a value of 0.1 for each increase in freestream velocity. Grey-shaded patches indicate the uncertainty interval $C_p \pm 2\,\%$. Note that the grey markers at the downstream end of the working section signify the region influenced by the over-pressure mesh; hence, these data were excluded from the assessment.

ZPG conditions. Owing to the relatively large cross-sectional area of the working section, the pressure coefficient is not sensitive to small variations in the ceiling height. The indicated $C_p \pm 2\,\%$ (grey shaded area) corresponds to changes in the ceiling height of approximately $\pm$ 5 mm, which exceeds the $\sim$ 1 mm accuracy in setting the ceiling profile.

4.5. Mean velocity profiles and integral parameters

Fig. 8 presents the inner-scaled mean streamwise velocity profiles for all Re_τ conditions, obtained from HWA (blue, square markers), PIV (yellow, plus markers), and PTV (purple, circle markers) measurements. Both the HWA and PIV measurements captured the full wall-normal extent of the TBL, of which we obtained the boundary layer characteristics employing a composite profile fit (sequential quadratic programming), using the log-layer constants $\kappa = 0.384$ and $B = 4.17$ [25]. Specifically, we obtain δ, Π, U_τ from the composite fit, where Π is the wake parameter. An uncertainty of $U_\tau \pm 0.7\%$ is assumed, based on the 95 % confidence interval reported for this method by Rodríguez-López et al. [33]. For the PTV data, the skin-friction velocity is directly determined from a linear fit to the data points residing in the region $1 \leq y^+ \leq 4.5$. Following the method by Knoop et al. [34], the uncertainty is determined based on the standard error of the linear fit and Student's t-distribution for small sample sizes to obtain the 95 % confidence interval. The numerical integration of the data points was used to obtain the displacement thickness, δ^*, and the momentum thickness, θ. Table 4 provides an overview of the relevant boundary layer parameters, inferred from the data corresponding to the three different measurement methods. At the highest velocity this manuscript considers ($U_\infty \approx 20$ m/s), a friction Reynolds number of $Re_\tau \approx 5\,100$ is achieved. At the same time, the viscous length scale is kept within the measurable range at $\sim$ 23 µm.

The full wall-normal extent of the mean velocity profiles, from the HWA and PIV experiments, are compared to a profile from a direct numerical simulation (DNS) of a TBL flow at $Re_\tau \approx 2\,000$ obtained from Sillero et al. [35]. A match of the experimental and DNS data in the inner-layer reflects a canonical ZPG TBL, whereas the deviation from the DNS in the outer-layer can be attributed to the differences in Re_τ.

To further evaluate the canonical behaviour of the ZPG TBL, we present in Fig. 9 the variation with $Re_x \equiv U_\infty x'/\nu$ of the skin friction coefficient, $C_f \equiv 2(U_\tau/U_\infty)^2$, the shape factor, $H \equiv \delta^*/\theta$, and the momentum thickness Reynolds number, $Re_\theta \equiv U_\infty \theta/\nu$. Comparisons between the experimental data and canonical scaling laws from the literature are made, details of which are included in the caption of Fig. 9. Skin friction

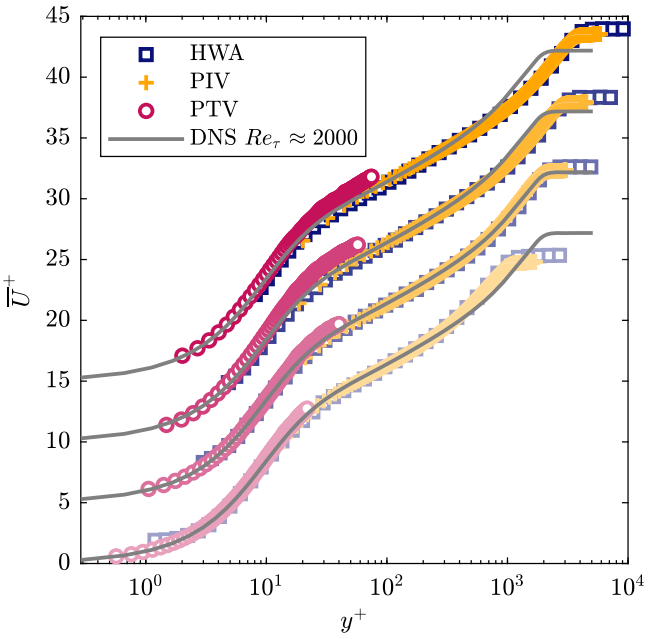

Fig. 8. Mean streamwise velocity profiles for the Reynolds number range of $Re_\tau \approx 1\,400$ to $5\,100$. An inner-scaling of the data is applied using the U_τ values of the respective techniques presented in Table 4. Profiles are consecutively offset in the vertical direction with a value of 5 for each increase in Re_τ. The profile of the DNS data corresponds to a TBL simulation at $Re_\tau \approx 2\,000$ [35] and is added onto all measured profiles for reference.

coefficients (obtained via HWA, PIV, and PTV) in Fig. 9(a) are compared to the scaling law by Schlichting and Gersten [36], which was later refitted by Nagib et al. [37] to a wide range of independent OFI experiments spanning beyond the range of our experimental data. A general agreement of our data with this refitted scaling law can be observed. The deviation of C_f values from different measurement techniques is attributed to the uncertainty (outside of the statistical 95 % confidence interval) of determining U_τ from each of the datasets. To give the reader an idea of the variation, we include the dashed line indicating $U_\tau \pm 2\,\%$. As for the other two indicators (H and Re_θ, in Fig. 9(b,c), respectively), these are not dependent on the friction velocity but rather on the integral scales of the TBL, *i.e.*, δ^* and θ. Chauhan et al. [25] proposed the shape factor, H, as a reliable metric to assess the quality of a ZPG TBL, in contrast to Reynolds number trends of Π, which showed a significant scatter among the ten ZPG TBL datasets used in their study. In fact, they revealed that for the majority of the data, H varies $\pm 2\,\%$ from the indicated scaling law, whereas Fig. 9(b) shows that the current H values are confined to $\pm 1\,\%$ (as indicated by the dotted lines). Lastly, a scaling law by Nagib et al. [37] is employed to validate Re_θ, which is derived from a large experimental dataset encompassing the present range of Re_x. Fig. 9(c) illustrates that the trend between Re_x and Re_θ closely aligns with its canonical behaviour.

4.6. Second-order turbulence statistics

We consider wall-normal profiles of Reynolds stresses and streamwise energy spectra as second-order statistics. Wall-normal profiles of the streamwise Reynolds stress, $\overline{uu}$, are presented in Fig. 10(a) for all Re_τ conditions and by considering the HWA and PIV data. Note that we adopt the same colour and marker styles as previously introduced in Figs. 8 and 9. We again include the DNS data from Sillero et al. [35] for reference. At the inner-peak location of $y^+ = 15$ (denoted by the vertical dashed line), the HWA data is subject to an attenuation of energy in relation to the DNS profile. This attenuation is ascribed to spatial filtering effects caused by the HWA probe's relatively long wire length [22].

Table 4
Overview of the ZPG TBL characteristics across the HWA, PIV, and PTV measurement techniques: note that only the inner scaling parameters could be obtained for the PIV method due to the limited wall-normal extent of the FOV.

Method	U_∞ (m/s)	Re_x	Re_τ	Re_θ	δ (mm)	δ^* (mm)	θ (mm)	Π	U_τ (m/s)	l_v (μm)	t_v (μs)
HWA	5.0	2.2×10^6	1 400	3 400	108	14.6	10.6	0.439	0.197 ± 0.0014	77.7	394.1
	9.9	4.4×10^6	2 800	7 500	120	15.8	11.7	0.533	0.359 ± 0.0025	42.8	119.1
	14.9	6.5×10^6	4 000	10 600	119	14.7	11.1	0.488	0.525 ± 0.0037	29.4	56.1
	19.8	8.6×10^6	5 100	13 700	119	14.4	10.9	0.487	0.684 ± 0.0048	23.0	33.7
PIV	4.6	2.1×10^6	1 400	3 100	109	13.7	10.0	0.351	0.185 ± 0.0013	80.8	437.9
	9.2	4.1×10^6	2 400	6 500	108	14.6	10.7	0.543	0.335 ± 0.0023	44.9	133.9
	13.7	6.2×10^6	3 600	9 200	108	13.5	10.1	0.470	0.492 ± 0.0034	30.5	62.0
	18.3	8.3×10^6	4 600	12 000	108	13.1	9.8	0.477	0.641 ± 0.0045	23.3	36.4
PTV	4.6	2.1×10^6	–	–	–	–	–	–	0.180 ± 0.0003	83.9	464.4
	9.2	4.1×10^6	–	–	–	–	–	–	0.327 ± 0.0014	45.2	135.4
	13.7	6.2×10^6	–	–	–	–	–	–	0.487 ± 0.0073	32.2	68.2
	18.3	8.3×10^6	–	–	–	–	–	–	0.628 ± 0.0161	23.7	36.9

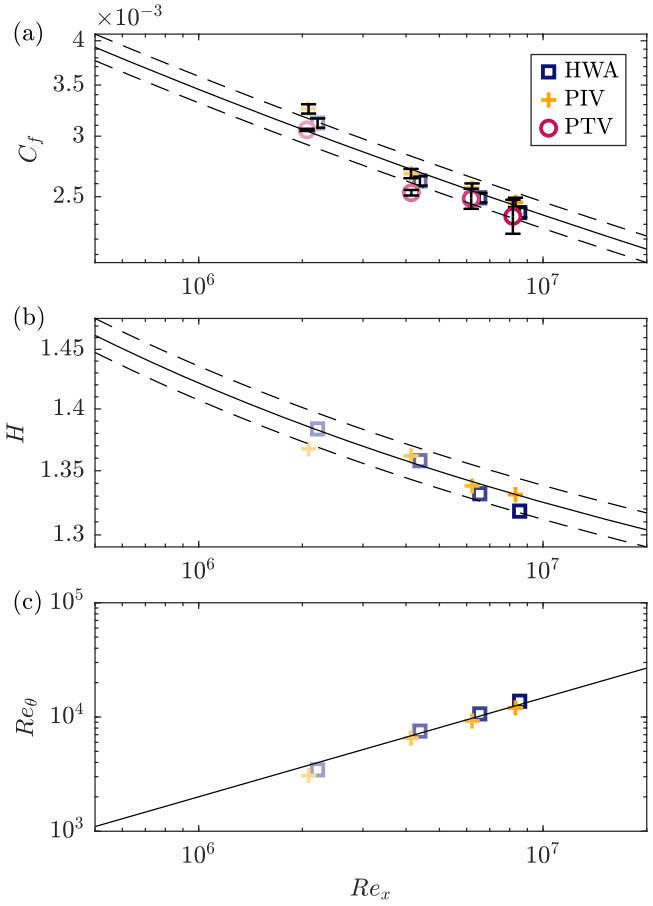

Fig. 9. Variation with Re_x of (a) the skin friction coefficient, errorbars denote the 95 % confidence interval; Solid line: Schlichting's relation $C_f = [2\log_{10}(Re_x) - 0.65]^{-7/3}$ [37]; Dashed lines: $U_\tau \pm 2\,\%$. (b) The shape factor H; Solid line: scaling law $H = (1 - 7.2/\sqrt{C_f})^{-1}$ [25]; Dashed lines: $H \pm 1\,\%$. (c) The momentum thickness Reynolds number; Solid line: power-law $Re_\theta = 0.01277 Re_x^{0.8659}$ [37].

Shown with the solid blue lines, the spatial filtering effect is corrected for following the method outlined by Smits et al. [38]. Their relation (3.8) is used and considers measured, attenuated inner-peak magnitudes of $\overline{uu}$. The growth of the inner-peak magnitude with Re_τ, relative to the reference profile of DNS at $Re_\tau \approx 2\,000$, is now captured. In fact, the corrected data closely follow the scaling law for the inner-peak magnitude proposed by Chen and Sreenivasan [39], $\overline{uu}^+_{peak} = 46\left(0.25 - 0.42/Re_\tau^{0.25}\right)$, shown with the cross markers. In the outer-layer ($y^+ \gtrsim 100$), the streamwise Reynolds stress increases with friction Reynolds number, a trend well captured by both PIV and HWA, demonstrating strong agreement between the two methods.

Fig. 10(b) displays wall-normal profiles of the Reynolds stresses, $\overline{uv}$ and $\overline{vv}$, obtained through PIV for various Reynolds numbers, with DNS data provided for reference. In the outer region of the TBL, an increase in the absolute values of Reynolds stresses is evident with rising Re_τ, which is typical for wall-bounded flows [40–42].

Based on the HWA data, Fig. 11(a) presents the energy spectrograms of the streamwise velocity, $\phi_{uu}(f, y)$, with two isocontour levels of $f^+\phi^+_{uu} = [0.4,\ 1.5]$. We can observe that the location of the inner-spectral peak is well-resolved across all friction Reynolds numbers, appearing at the expected location $(f^+; y^+) = (0.01; 15)$. To further assess the streamwise velocity spectra, Fig. 11(b) presents the spectra at $y^+ \approx 15$ for all Re_τ conditions. As observed previously, an increase in the friction Reynolds number leads to a reduction in the magnitude of the inner-spectral peak, again attributed to the spatial filtering due to the finite-length hot-wire sensor. Moreover, we observe an increase in low-frequency energy correlated with Re_τ in Fig. 11(c), where the streamwise velocity spectra at $y^+ = 200$ are presented. This increase in energy of the outer-spectral peak corresponds to an energisation of the LSMs and VLSMs [3] and the growing range of energetic turbulent scales at higher Re_τ conditions.

4.7. Wall-pressure spectra

We assess the wall-pressure spectrum to assess whether the hydrodynamic, TBL-induced pressure fluctuations can be resolved. Generally, wall-pressure measurements are of interest in this facility from the perspective of, for instance, using wall-pressure as input to flow estimators for flow control schemes [28,43].

Fig. 12 presents the premultiplied wall-pressure spectra, $f\phi_{p_w p_w}$, for all Re_τ conditions. Our experimental spectra are compared with the wall-pressure spectrum from a DNS of turbulent channel flow at $Re_\tau \approx 2\,000$ obtained from Lee and Moser [41]. The resonance frequency of the pinhole–cavity configuration (recall Section 3.3) coincides with a range where pressure fluctuations remain energetic for the three highest Reynolds numbers ($Re_\tau \approx 2\,800$ to $5\,100$). Despite applying a Helmholtz correction in the frequency domain, the experimental wall-pressure spectra exhibit an overshoot within the small-scale range. This intensification of energy is related to the imperfect correction with the Helmholtz transfer kernel's gain—the gain was derived from an acoustic experiment without effects of the grazing flow being present [this is a common issue in case the resonance frequency overlaps with the energetic frequencies of the turbulence, see 44]. The frequency range where

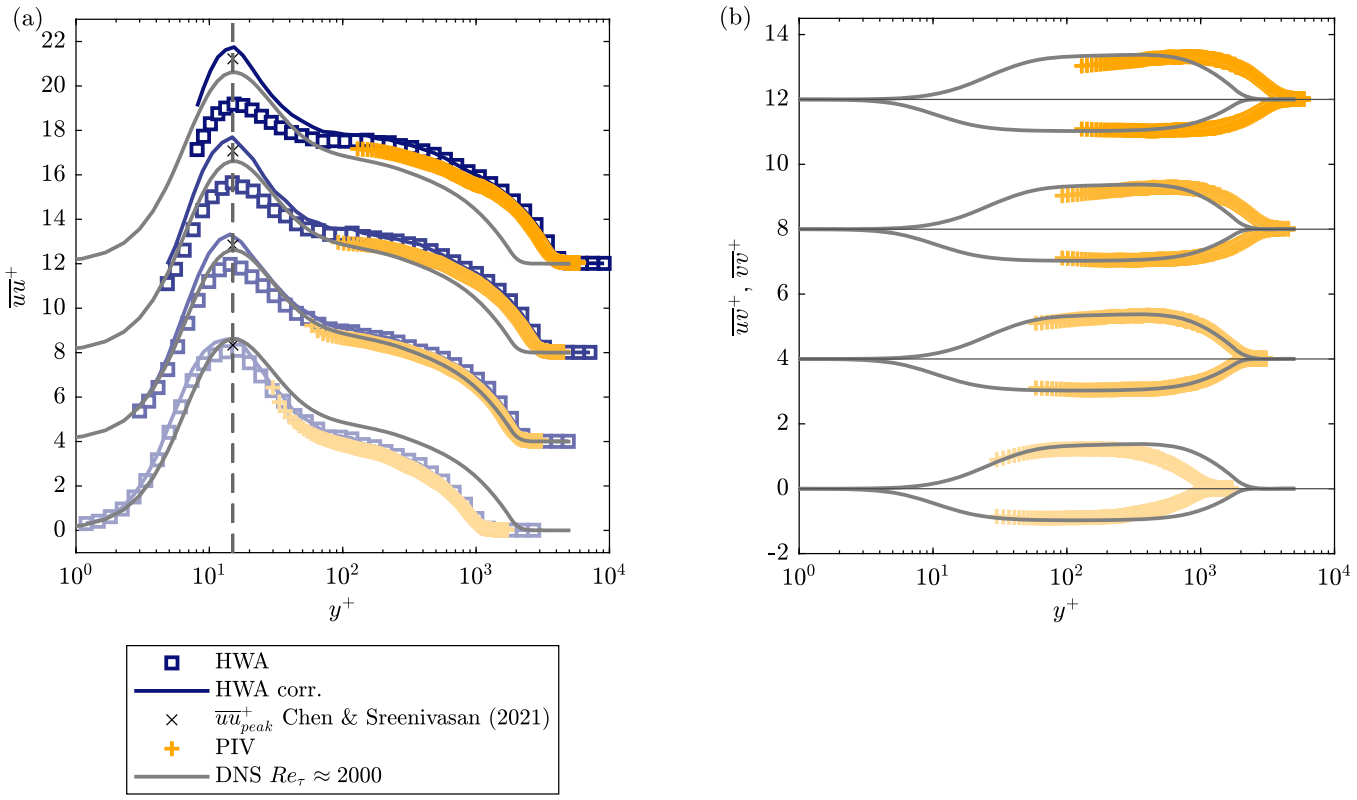

Fig. 10. (a) Wall-normal profiles of the streamwise Reynolds stress $\overline{uu}^+$ for the Reynolds number range of $Re_\tau \approx 1\,400$ to $5\,100$. The HWA data are corrected (solid blue lines) following Smits et al. [38] and compared to $\overline{uu}^+_{peak}$ values (x-markers) taken from the scaling law proposed by Chen and Sreenivasan [39]. (b) Wall-normal profiles of the wall-normal and shear Reynolds stresses, $\overline{vv}^+$ and $\overline{uv}^+$, respectively. In both (a) and (b) the profiles are consecutively offset in the vertical direction with a value of 4 for each increase in Re_τ. Profiles of the DNS data correspond to a TBL simulation at $Re_\tau \approx 2\,000$ [35] and are added onto all measured profiles for reference. (For interpretation of the references to colour in this figure legend, the reader is referred to the web version of this article.)

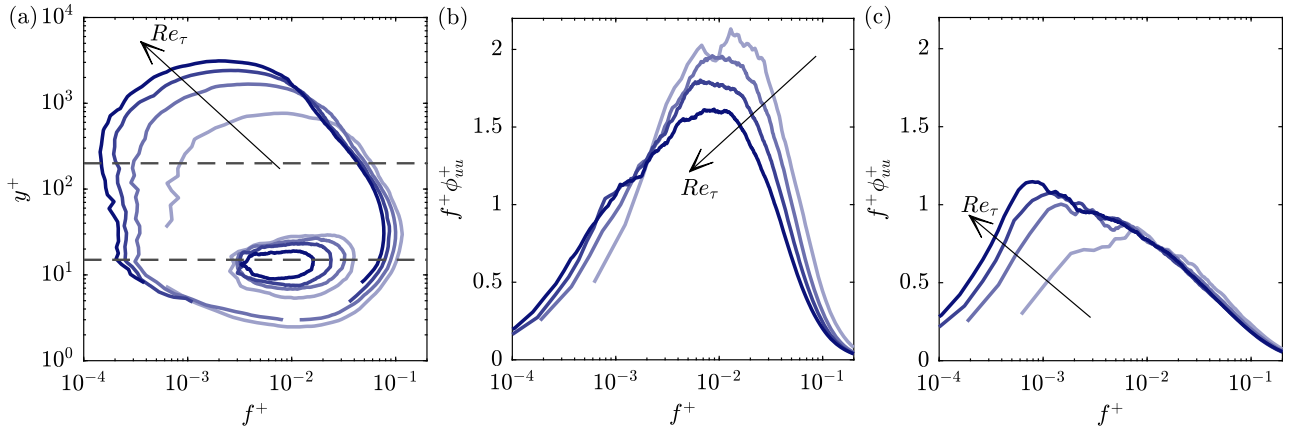

Fig. 11. (a) Premultiplied energy spectrogram of the streamwise velocity fluctuations, $f^+\phi^+_{uu}$, obtained from the HWA data for the Reynolds number range of $Re_\tau \approx 1\,400$ to $5\,100$; two isocontour levels are shown: $f^+\phi^+_{uu} = [0.4,\ 1.5]$. The two horizontal dashed lines in (a) correspond to the locations for which the spectra are presented in sub-figure (b) $y^+ \approx 15$, and (c) $y^+ \approx 200$, respectively.

data reliability is limited due to the influence of the pinhole–cavity resonance is highlighted with the light-shaded grey lines and the circles signifying the onset of this frequency range.

When inspecting the resolved portions of the wall-pressure spectra, it is evident that the low-frequency energy increases with higher values of Re_τ. Additionally, the magnitude of the inner-spectral peak slightly grows as the friction Reynolds number increases from $Re_\tau \approx 1\,400$ to $Re_\tau \approx 2\,800$. A main difference between the experimental spectra and the spectrum of the DNS of turbulent channel flow is that the former is more energetic, especially in the frequency range centred around the location of the inner-spectral peak ($f^+ = 0.04$). This observation aligns with findings reported in the literature [40,44]; note that the comparison is also for qualitative purposes only, as the flow geometry is different (experimental TBL flow versus DNS of channel flow) and the DNS spectrum is a spatial spectrum (converted into a temporal spectrum using using $f^+ = U_c^+/\lambda_x^+$, with $U_c^+ = 10$).

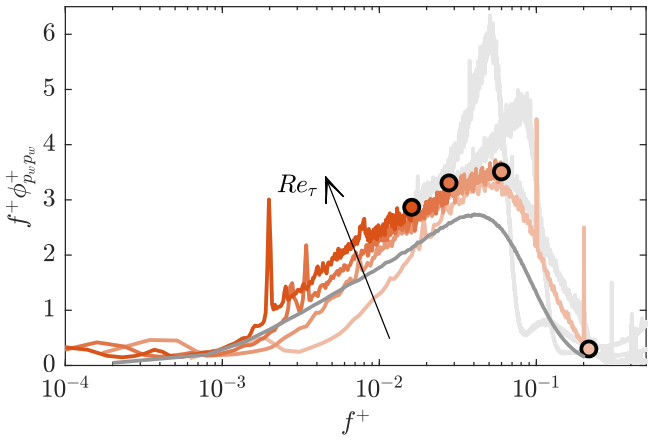

Fig. 12. Premultiplied wall-pressure spectrum $f^+\phi^+_{p_w\ p_w}$ for the Reynolds number range of $Re_\tau \approx 1\,400$ to $5\,100$. Data are compared to a wall-pressure spectrum obtained from a DNS of turbulent channel flow at $Re_\tau \approx 2\,000$ [41]; note that the wavelength spectrum from the DNS is converted into frequency spectrum using $f^+ = U_c^+/\lambda_x^+$, with $U_c^+ = 10$. Additionally, the light-shaded grey lines signify the frequency range corresponding to unreliable data due to the pinhole–cavity resonance, and the circles signify the onset of this high-frequency range.

5. Concluding remarks

The development of the DU-BLF was motivated by attaining a moderate friction Reynolds number for studying TBL flows with a sufficient scale separation. A ZPG TBL facility was developed, with the working section comprising a streamwise extent of ~ 7.2 m, double that of a previous boundary layer facility at the Delft University of Technology [6]. While the current scope was to present the flow characteristics associated with a TBL flow developing under a zero (streamwise) pressure gradient, the design of the working section allows for boundary layer research under a variety of conditions, *e.g.*, with different streamwise pressure gradients, and/or with flow control efforts via active or passive methods. Moreover, there is physical access along the full streamwise extent of the working section, while its polycarbonate walls permit full accessibility for optical measurement techniques.

Regarding the general flow characteristics related to the tunnel facility, we established that the turbulence intensity is low with an intensity less than $\sim 0.1\,\%$. For the TBL flow study, the flow developed under a nominally zero (streamwise) pressure gradient over its entire development length. Measurements conducted at freestream velocities ranging from $U_\infty \approx 5$ to 20 m/s provided validation data from which it was concluded that the boundary layer adheres to the established trend for canonical ZPG TBL flow. Under these conditions, a moderately-high friction Reynolds number is attained in the downstream part of the section, ranging from $Re_\tau \approx 1\,400$ to $5\,100$.

CRediT authorship contribution statement

Max W. Knoop: Writing – original draft, Writing – review & editing, Visualisation, Methodology, Investigation, Formal analysis, Conceptualisation; **Abdelrahman Hassanein:** Writing – original draft, Writing – review & editing, Visualisation, Methodology, Investigation, Formal analysis, Conceptualisation; **Woutijn J. Baars:** Writing – original draft, Writing – review & editing, Supervision, Funding acquisition, Conceptualisation.

Data availability

A full dataset of the ZPG TBL will be made available online [45]. The dataset includes the statistical wall-normal profiles obtained via HWA, PIV and PTV, accompanied by the relevant ambient conditions, scaling parameters and TBL characteristics (as provided in Table 4). In addition, we provide the time series of the conducted HWA measurements, freestream acoustic pressure measurements, and wall-pressure measurements, respectively.

Declaration of competing interest

The authors declare that they have no known competing financial interests or personal relationships that could have appeared to influence the work reported in this paper.

Acknowledgement

We express our appreciation to T. van Leeuwen for leading the CAD design phase of the working section of the DU-BLF, together with W.J. Baars (current co-author) and M. van Nesselrooij (Dimple Aerospace B.V.). In addition, we acknowledge the Department of Electronic and Mechanical Development (DEMO) for assisting with the design phase of the facility, in particular, P. Posthoorn. For technical support and advice, we would like to give special thanks to the personnel of the Flow Physics & Technology laboratory, especially S. Bernardy, E. Langedijk, H.-J. Siemer and F.F.J. Schrijer. We thank A.D. Sequeira for conducting the open-jet characterisation and sharing the experimental data.

For commencing the DU-BLF, we gratefully acknowledge financial support provided by the European Office of Aerospace Research and Development (EOARD) of the U.S. Air Force Office of Scientific Research (AFOSR) under award number FA8655-22-1-7168, and by the Netherlands Enterprise Agency under grant number TSH21002.

References

[1] J. Jiménez, Cascades in wall-bounded turbulence, Annu. Rev. Fluid Mech. 44 (Volume 44, 2012) (2012) 27–45. https://doi.org/10.1146/annurev-fluid-120710-101039
[2] N. Kasagi, Y. Suzuki, K. Fukagata, Microelectromechanical systems–based feedback control of turbulence for skin friction reduction, Annu. Rev. Fluid Mech. 41 (1) (2009) 231–251. https://doi.org/10.1146/annurev.fluid.010908.165221
[3] N. Hutchins, I. Marusic, Large-scale influences in near-wall turbulence, Phil. Trans. R. Soc. A 365 (2007) 647–64. https://doi.org/10.1098/rsta.2006.1942
[4] B.J. McKeon, The engine behind (wall) turbulence: perspectives on scale interactions, J. Fluid Mech. 817 (2017) P1. https://doi.org/10.1017/jfm.2017.115
[5] M.R. Abbassi, W.J. Baars, N. Hutchins, I. Marusic, Skin-friction drag reduction in a high-Reynolds-number turbulent boundary layer via real-time control of large-scale structures, Int. J. Heat Fluid Flow 67 (2017) 30–41. https://doi.org/10.1016/j.ijheatfluidflow.2017.05.003
[6] G. Dacome, R. Mörsch, M. Kotsonis, W.J. Baars, Opposition flow control for reducing skin-friction drag of a turbulent boundary layer, Phys. Rev. Fluids 9 (6) (2024) 064602. https://doi.org/10.1103/PhysRevFluids.9.064602
[7] J.M. Österlund, Experimental Studies of Zero Pressure-Gradient Turbulent Boundary Layer Flow, Ph.D. thesis, KTH, 1999.
[8] M. Aguiar Ferreira, P. Costa, B. Ganapathisubramani, Wall shear stress measurement using a zero-displacement floating-element balance, Exp. Fluids 65 (4) (2024) 56. https://doi.org/10.1007/s00348-024-03785-1
[9] I. Marusic, K.A. Chauhan, V. Kulandaivelu, N. Hutchins, Evolution of zero-pressure-gradient boundary layers from different tripping conditions, J. Fluid Mech. 783 (2015) 379–411. https://doi.org/10.1017/jfm.2015.556
[10] A. Talamelli, F. Persiani, J.H.M. Fransson, P.H. Alfredsson, A.V. Johansson, H.M. Nagib, J.-D. Rüedi, K.R. Sreenivasan, P.A. Monkewitz, CICLoPE-a response to the need for high Reynolds number experiments, Fluid Dyn. Res. 41 (2) (2009) 021407. https://doi.org/10.1088/0169-5983/41/2/021407
[11] G. Bellani, A. Talamelli, The final design of the long pipe in CICLoPE, Prog. in Turb. VI (2016) 205–209. https://doi.org/10.1007/978-3-319-29130-7_36
[12] R. Örlü, T. Fiorini, A. Segalini, G. Bellani, A. Talamelli, P.H. Alfredsson, Reynolds stress scaling in pipe flow turbulence-first results from CICLoPE, Phil. Trans. R. Soc. A. 375 (2017) 20160187. https://doi.org/10.1098/rsta.2016.0187
[13] F. König, E.-S. Zanoun, E. Öngüner, C. Egbers, The CoLaPipe-the new Cottbus large pipe test facility at Brandenburg university of technology Cottbus-Senftenberg, Rev. Sci. Instrum. 85 (7) (2014) 075115. https://doi.org/10.1063/1.4884717
[14] N. Furuichi, Y. Terao, Y. Wada, Y. Tsuji, Friction factor and mean velocity profile for pipe flow at high Reynolds numbers, Phys. Fluids 27 (9) (2015) 095108. https://doi.org/10.1063/1.4930987
[15] M. Hultmark, M. Vallikivi, S.C.C. Bailey, A.J. Smits, Turbulent pipe flow at extreme Reynolds numbers, Phys. Rev. Lett. 108 (2012) 094501. https://doi.org/10.1103/PhysRevLett.108.094501
[16] J. Carlier, M. Stanislas, Experimental study of eddy structures in a turbulent boundary layer using particle image velocimetry, J. Fluid Mech. 535 (2005) 143–188. https://doi.org/10.1017/S0022112005004751

[17] M. Samie, I. Marusic, N. Hutchins, M.K. Fu, Y. Fan, M. Hultmark, A.J. Smits, Fully resolved measurements of turbulent boundary layer flows up to $Re_\tau = 20\,000$, J. Fluid Mech. 851 (2018) 391–415. https://doi.org/10.1017/jfm.2018.508
[18] A.J. Smits, B.J. McKeon, I. Marusic, High-Reynolds number wall turbulence, Annu. Rev. Fluid Mech. 43 (2011) 353–375. https://doi.org/10.1146/annurev-fluid-122109-160753
[19] J. Jiménez, Coherent structures in wall-bounded turbulence, J. Fluid Mech. 842 (2018) P1. https://doi.org/10.1017/jfm.2018.144
[20] B.F.A. van Hest, Laminar-Turbulent Transition in Boundary Layers with Adverse Pressure Gradient, Ph.D. thesis, Delft University of Technology, 1996. https://resolver.tudelft.nl/uuid:bd54ed1a-a450-456c-bb95-d89a64695bbf.
[21] M. Van Nesselrooij, O.W.G. Van Campenhout, B.W. Van Oudheusden, F.F.J. Schrijer, L.L.M. Veldhuis, Development of an experimental apparatus for flat plate drag measurements and considerations for such measurements, Meas. Sci. Technol. 33 (5) (2022) 055303. https://doi.org/10.1088/1361-6501/ac527f
[22] N. Hutchins, T.B. Nickels, I. Marusic, M.S. Chong, Hot-wire spatial resolution issues in wall-bounded turbulence, J. Fluid Mech. 635 (2009) 103–136. https://doi.org/10.1017/S0022112009007721
[23] M. Hultmark, A.J. Smits, Temperature corrections for constant temperature and constant current hot-wire anemometers, Meas. Sci. Technol. 21 (10) (2010) 105404. https://doi.org/10.1088/0957-0233/21/10/105404
[24] R. Örlü, J.H.M. Fransson, P.H. Alfredsson, On near wall measurements of wall bounded flows-the necessity of an accurate determination of the wall position, Prog. Aerosp. Sci. 46 (8) (2010) 353–387. https://doi.org/10.1016/j.paerosci.2010.09.001
[25] K.A. Chauhan, P.A. Monkewitz, H.M. Nagib, Criteria for assessing experiments in zero pressure gradient boundary layers, Fluid Dyn. Res. 41 (2) (2009) 021404. https://doi.org/10.1088/0169-5983/41/2/021404
[26] F. Scarano, M.L. Riethmuller, Advances in iterative multigrid PIV image processing, Exp. Fluids 29 (Suppl 1) (2000) S051–S060. https://doi.org/10.1007/s003480070007
[27] F. Scarano, Iterative image deformation methods in PIV, Meas. Sci. Technol. 13 (1) (2001) R1. https://doi.org/10.1088/0957-0233/13/1/201
[28] W.J. Baars, G. Dacome, M. Lee, Reynolds-number scaling of wall-pressure-velocity correlations in wall-bounded turbulence, J. Fluid Mech. 981 (2024) A15. https://doi.org/10.1017/jfm.2024.46
[29] A.F. Rius-Vidales, M. Kotsonis, Impact of a forward-facing step on the development of crossflow instability, J. Fluid Mech. 924 (2021) A34. https://doi.org/10.1017/jfm.2021.497
[30] R. Merino-Martínez, A.R. Carpio, L.T.L. Pereira, S. van Herk, F. Avallone, D. Ragni, M. Kotsonis, Aeroacoustic design and characterization of the 3D-printed, open-jet, anechoic wind tunnel of Delft university of technology, Appl. Acoust. 170 (2020) 107504. https://doi.org/10.1016/j.apacoust.2020.107504
[31] H. Görtler, Berechnung von aufgaben der freien turbulenz auf grund eines neuen näherungsansatzes, J. Appl. Math. Mech. 22 (5) (1942) 244–254.
[32] M.P. Schultz, K.A. Flack, The rough-wall turbulent boundary layer from the hydraulically smooth to the fully rough regime, J. Fluid Mech. 580 (2007) 381–405. https://doi.org/10.1017/S0022112007005502
[33] E. Rodríguez-López, P.J.K. Bruce, O.R.H. Buxton, A robust post-processing method to determine skin friction in turbulent boundary layers from the velocity profile, Exp. Fluids 56 (2015) 1–16. https://doi.org/10.1007/s00348-015-1935-5
[34] M.W. Knoop, F.H. Hartog, F.F.J. Schrijer, O.W.G. van Campenhout, M. van Nesselrooij, B.W. van Oudheusden, Experimental assessment of square-wave spatial spanwise forcing of a turbulent boundary layer, Exp. Fluids 65 (5) (2024) 65. https://doi.org/10.1007/s00348-024-03799-9
[35] J.A. Sillero, J. Jiménez, R.D. Moser, One-point statistics for turbulent wall-bounded flows at Reynolds numbers up to $\delta^+ \approx 2000$, Phys. Fluids 25 (10) (2013) 105102. https://doi.org/10.1063/1.4823831
[36] H. Schlichting, K. Gersten, Boundary-Layer Theory, Springer, 2016.
[37] H.M. Nagib, K.A. Chauhan, P.A. Monkewitz, Approach to an asymptotic state for zero pressure gradient turbulent boundary layers, Phil. Trans. R. Soc. A 365 (1852) (2007) 755–770. https://doi.org/10.1098/rsta.2006.1948
[38] A.J. Smits, J. Monty, M. Hultmark, S.C.C. Bailey, N. Hutchins, I. Marusic, Spatial resolution correction for wall-bounded turbulence measurements, J. Fluid Mech 676 (2011) 41–53. https://doi.org/10.1017/jfm.2011.19
[39] X. Chen, K.R. Sreenivasan, Reynolds number scaling of the peak turbulence intensity in wall flows, J. Fluid Mech. 908 (2021) R3. https://doi.org/10.1017/jfm.2020.991
[40] J. Jiménez, S. Hoyas, M.P. Simens, Y. Mizuno, Turbulent boundary layers and channels at moderate Reynolds numbers, J. Fluid Mech. 657 (2010) 335–360. https://doi.org/10.1017/S0022112010001370
[41] M. Lee, R.D. Moser, Direct numerical simulation of turbulent channel flow up to $Re_\tau \approx 5200$, J. Fluid Mech. 774 (2015) 395–415. https://doi.org/10.1017/jfm.2015.268
[42] S. Hoyas, M. Oberlack, F. Alcántara-Ávila, S.V. Kraheberger, J. Laux, Wall turbulence at high friction Reynolds numbers, Phys. Rev. Fluids 7 (1) (2022) 014602. https://doi.org/10.1103/PhysRevFluids.7.014602
[43] G. Dacome, Real-Time Control of Wall-Bounded Turbulence, Ph.D. thesis, Delft University of Technology, Delft, The Netherlands, 2025.
[44] G. Dacome, L. Lazzarini, A. Talamelli, G. Bellani, W.J. Baars, Scaling of wall-pressure–velocity correlations in high Reynolds number turbulent pipe flow, J. Fluid Mech. 1013 (2025) A48.
[45] M.W. Knoop, A. Hassanein, W.J. Baars, Dataset underlying the publication: development and characterisation of a turbulent boundary layer facility at the Delft university of technology, 2025, https://doi.org/10.4121/d0af5e8b-6bde-4c02-a165-c752b5ab435a